


 Cite this: *RSC Adv.*, 2020, **10**, 865

In vivo neutron capture therapy of cancer using ultrasmall gadolinium oxide nanoparticles with cancer-targeting ability†

Son Long Ho, [‡]^a Garam Choi, [‡]^b Huan Yue, ^a Hee-Kyung Kim, ^b Ki-Hye Jung, ^c Ji Ae Park, ^c Mi Hyun Kim, ^c Yong Jin Lee, ^c Jung Young Kim, ^c Xu Miao, ^a Mohammad Yaseen Ahmad, ^a Shanti Marasini, ^a Adibehalsadat Ghazanfari, ^a Shuwen Liu, ^a Kwon-Seok Chae, ^d Yongmin Chang ^{*b} and Gang Ho Lee ^{*a}

Gadolinium neutron capture therapy (GdNCT) is considered as a new promising cancer therapeutic technique. Nevertheless, limited GdNCT applications have been reported so far. In this study, surface-modified ultrasmall gadolinium oxide nanoparticles (UGNPs) with cancer-targeting ability ($d_{avg} = 1.8$ nm) were for the first time applied to the *in vivo* GdNCT of cancer using nude model mice with cancer, primarily because each nanoparticle can deliver hundreds of Gd to the cancer site. For applications, the UGNPs were grafted with polyacrylic acid (PAA) for biocompatibility and colloidal stability, which was then conjugated with cancer-targeting arginylglycylaspartic acid (RGD) (shortly, RGD-PAA-UGNPs). The solution sample was intravenously administered into the tails of nude model mice with cancer. At the time of the maximum accumulation of the RGD-PAA-UGNPs at the cancer site, which was monitored using magnetic resonance imaging, the thermal neutron beam was locally irradiated onto the cancer site and the cancer growth was monitored for 25 days. The cancer growth suppression was observed due to the GdNCT effects of the RGD-PAA-UGNPs, indicating that the surface-modified UGNPs with cancer-targeting ability are potential materials applicable to the *in vivo* GdNCT of cancer.

Received 31st October 2019
 Accepted 17th December 2019

DOI: 10.1039/c9ra08961f
rsc.li/rsc-advances

Introduction

Surface-modified ultrasmall gadolinium (Gd) oxide nanoparticles (UGNPs) with cancer-targeting ability are potential candidate materials for cutting-edge theragnostic applications due to their excellent water proton relaxivities^{1–4} and the very high thermal neutron beam capture cross sections (σ) of Gd.^{5–9} Their cancer-targeting ability will boost their performance. In addition, their ultrasmall size is suitable for both intravenous (IV) administration and renal excretion.^{10–12}

Gadolinium neutron capture therapy (GdNCT) as a non-invasive and combined cancer therapeutic technique of using

Gd-chemicals and a thermal neutron beam requires accumulation of a sufficient amount of Gd at the cancer site.^{13,14} Considering that the surface-modified UGNPs with cancer-targeting ability can deliver hundreds of Gd per nanoparticle to the cancer site, they may be ideal materials for GdNCT, but have not been tried in GdNCT so far.

The underlying principle of GdNCT is as follows. Auger and Coster-Kronig (ACK) electrons or γ -ray or both generated from the ^{157}Gd (n, γ) ^{158}Gd nuclear reaction kill the cancer cells by damaging deoxyribonucleic acids (DNAs) in cancer cell nuclei.^{6,7} Considering the penetration depths of the ACK electrons (cell dimensions) and the γ -ray (>10 cm) and that the γ -ray would damage the normal cells as well as the cancer cells due to its long penetration depth, it is preferable for the ACK electrons to mainly contribute to the killing of the cancer cells. This could be achieved if Gd-chemicals could target and penetrate the cancer cells or preferably the cancer cell nuclei^{15,16} under low thermal neutron beam irradiation doses. The surface-modified UGNPs with cancer-targeting ability are suitable for this purpose because they can target and penetrate the cancer cells^{17–22} and can even penetrate the cancer cell nuclei due to their ultrasmall size.¹⁹

Among two branches in the NCT, the GdNCT has several advantages over the boron NCT (BNCT). First, although the natural abundance of 15.65% of ^{157}Gd is slightly lower than

^aDepartment of Chemistry, Department of Nanoscience and Nanotechnology (DNN), College of Natural Sciences, Kyungpook National University (KNU), Taegu 41566, South Korea. E-mail: ghlee@mail.knu.ac.kr

^bDepartment of Molecular Medicine and Medical & Biological Engineering, DNN, School of Medicine, KNU and Hospital, Taegu 41566, South Korea. E-mail: ychang@knu.ac.kr

^cDivision of RI-Convergence Research, Korea Institute of Radiological & Medical Science (KIRAMS), Seoul 08171, South Korea

^dDepartment of Biology Education, DNN, Teachers' College, KNU, Taegu 41566, South Korea

† Electronic supplementary information (ESI) available. See DOI: 10.1039/c9ra08961f

‡ These authors contributed equally.



19.9% of ^{10}B , ^{157}Gd has the highest σ value of 257 000 barns among the stable radionuclides in the periodic table, which is higher than 3840 barns of ^{10}B .⁵⁻⁷ In addition, ^{155}Gd with 14.8% in natural abundance also has a higher σ value of 60 700 barns than ^{10}B .^{5,7} Second, the Gd-chemicals can also serve as a diagnostic agent of cancer *via* magnetic resonance imaging (MRI),¹⁻⁴ making them useful as theragnostic agents of cancer *via* MRI and GdNCT, as recently demonstrated with Gd-chelate based materials.^{23,24}

Nevertheless, the GdNCT suffers from the lack of suitable Gd-chemicals, whereas two clinically applicable B-chemicals are available for BNCT.²⁵ Until now, only the commercial Gd-chelates and nanocomposites containing them have been applied to the *in vivo* GdNCT of cancer using cancer model mice^{23,24,26-32} and dogs.³³ However, they have shown limitations because commercial Gd-chelates are extracellular^{1,2} and not specific to cancer,^{1,2} and the nanocomposites are generally too big to be IV administered. Therefore, a breakthrough in Gd-chemicals is needed. The ideal materials for the *in vivo* GdNCT of cancer should deliver a large amount of Gd to the cancer site and penetrate the cancer cells. They should be also suitable for IV administration. The surface-modified UGNPs with cancer-targeting ability will be ideal materials to satisfy these conditions.

In this study, the surface-modified UGNPs with cancer-targeting ability were for the first time applied to the *in vivo* GdNCT of cancer using cancer model nude mice. To this end, the UGNPs were grafted with hydrophilic and biocompatible polyacrylic acid (PAA),³⁴ which was then conjugated with cancer-targeting arginylglycylaspartic acid (RGD)³⁵ (shortly, RGD-PAA-UGNP). In our previous study, the Rho-PAA-UGNPs (Rho = rhodamine B as a fluorescence imaging agent) were successfully applied to the *in vitro* GdNCT of human brain malignant glioma (U87MG) cells in which a significant cancer cell death that was 1.75 times higher than that obtained using the commercial Gd-chelate Gadovist was observed.³⁶ In this study, we further explored the *in vivo* GdNCT of cancer using the RGD-PAA-UGNPs with cancer-targeting ability to see their suitability in the *in vivo* GdNCT of cancer (see Fig. 1 for overall scheme of the *in vivo* GdNCT experiment).

Results and discussion

Particle diameter, hydrodynamic diameter, and crystal structure

High-resolution transmission electron microscopy (HRTEM) images are provided in two magnification scales (Fig. 2a and b). In general, the RGD-PAA-UGNPs were monodisperse and ultrasmall in particle diameter. An aqueous solution sample containing the RGD-PAA-UGNPs is provided as an inset in Fig. 2b (left vial), and it displays a good colloidal dispersion as confirmed using a visible light scattering (the Tyndall effect), whereas triple-distilled water had no light scattering (right vial). The average particle (d_{avg}) and hydrodynamic (a_{avg}) diameters of the RGD-PAA-UGNPs were estimated as 1.8 ± 0.1 and 12.1 ± 0.1 nm from log-normal function fits to the observed particle and hydrodynamic diameter distributions, respectively (Fig. 2c and d). The large value of a_{avg} was due to the polymer-

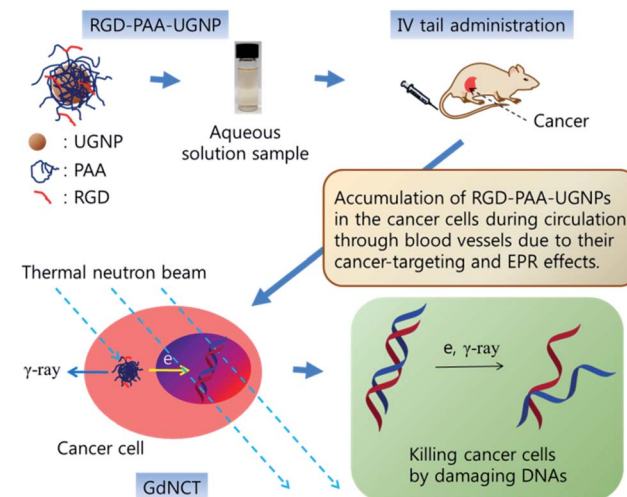


Fig. 1 Scheme of the *in vivo* GdNCT experiment. As indicated by arrows, the aqueous solution sample containing the RGD-PAA-UGNPs is IV administered into the nude mice tails; the RGD-PAA-UGNPs are accumulated into the cancer cells during the circulation through blood vessels by their cancer-targeting effect and enhanced permeability and retention (EPR) effect; and the ACK-electrons, γ -ray or both generated upon the absorption of the thermal neutrons by ^{157}Gd and ^{155}Gd damage DNAs inside the cancer cell nuclei, killing the cancer cells. The drawing scale is arbitrary.

coating^{37,38} and the origin for the good colloidal stability: the RGD-PAA-UGNPs did not settle down. X-ray diffraction (XRD) patterns before and after the thermogravimetric analysis (TGA) (Fig. S1 in ESI†) revealed that the as-prepared RGD-PAA-UGNPs were amorphous, due to their ultrasmall particle diameter,³⁹ whereas after TGA up to $900\text{ }^{\circ}\text{C}$, the nanoparticles exhibited a cubic structure of Gd_2O_3 with a cell constant of 10.82 \AA due to the particle size growth and crystallization,⁴⁰ which is consistent with the reported value.⁴¹

Surface-coating results

The surface-coating of the UGNPs was investigated by recording Fourier transform-infrared (FT-IR) absorption spectra of the RGD, PAA, PAA-UGNP, and RGD-PAA-UGNP powder samples pelletized in KBr (Fig. 3). The C=O stretch of the PAA appeared in the FT-IR absorption spectrum of the PAA-UGNPs, confirming the surface-coating of the UGNPs with the PAA. The C=O stretch at 1553 cm^{-1} in the FT-IR absorption spectrum of the PAA-UGNPs was red-shifted by 144 cm^{-1} from 1697 cm^{-1} of the free PAA due to the electrostatic bonds between the COO^- groups of each PAA and surface Gd^{3+} ions of each UGNP. Note that each PAA has many COO^- groups and thus, it can allow many electrostatic bonds with an UGNP through COO^- - Gd^{3+} interactions. This corresponds to the type of interaction between a hard acid (Gd^{3+}) and a hard base (COO^-).⁴²⁻⁴⁴ Similar red-shifts have previously been observed in many metal oxide nanoparticles coated with ligands containing carboxyl groups,⁴⁵⁻⁴⁸ supporting our result. The N-H bend at 1544 cm^{-1} and the C-N stretch at 1390 cm^{-1} of the RGD^{22,35} appeared in the FT-IR absorption spectrum of the RGD-PAA-UGNPs,



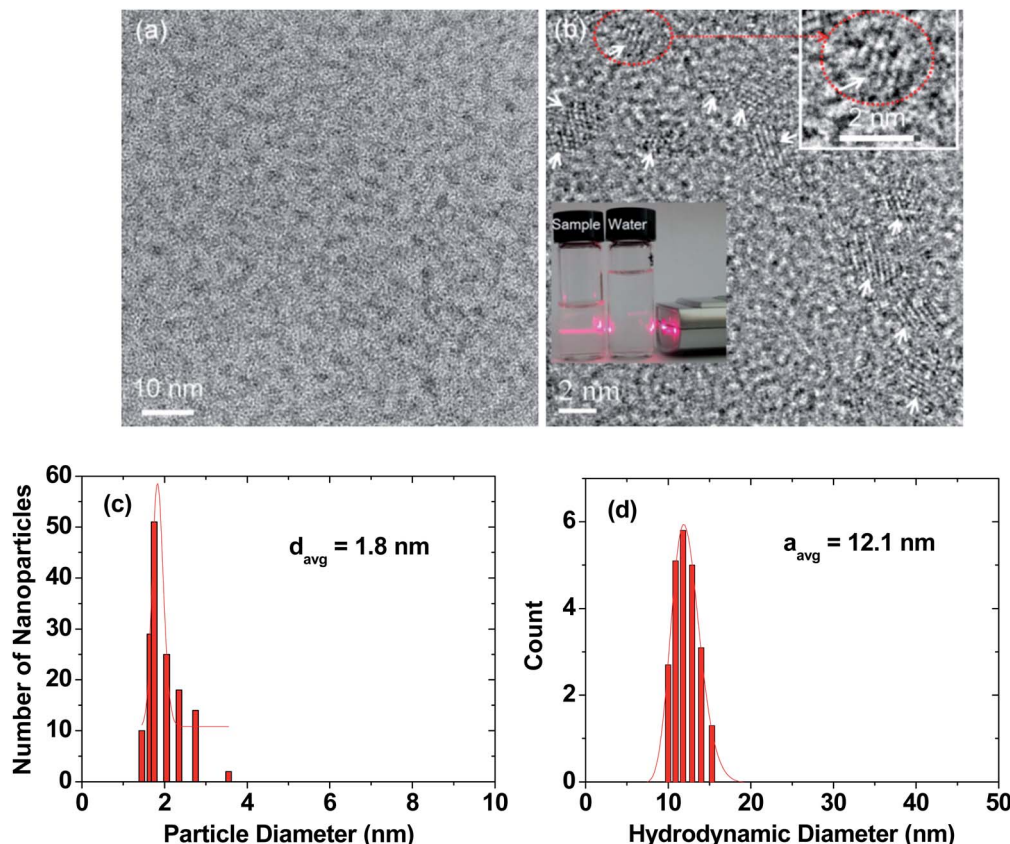


Fig. 2 Particle diameter and hydrodynamic diameter of RGD-PAA-UGNPs. (a) and (b) HRTEM images at different scales: arrows in (b) indicate nanoparticles, the dotted circle in (b) was magnified at the top-right portion of the image to clearly show a nanoparticle, and the visible light scattering in (b) confirms the RGD-PAA-UGNP dispersion in the aqueous solution by the Tyndall effect (left vial), whereas triple-distilled water (right vial) had no light scattering. (c) Particle diameter distribution with log-normal function fit, showing monodisperse and ultrasmall nanoparticles. (d) Hydrodynamic diameter distribution with log-normal function fit, showing monodisperse and large hydrodynamic diameter and thus, explaining the observed good colloidal stability.

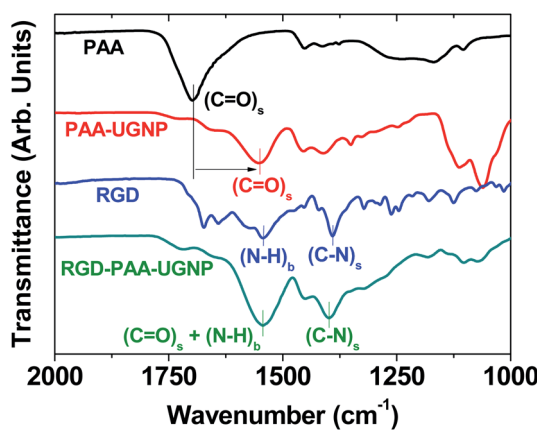


Fig. 3 FT-IR absorption spectra of the PAA, PAA-UGNP, RGD, and RGD-PAA-UGNP (the lowercases "s" and "b" indicate stretch and bend, respectively). In the FT-IR absorption spectrum of the PAA-UGNP, the C=O stretch (labelled using vertical bars) was red-shifted (indicated by an arrow) due to the bonding of carboxyl group of the PAA to surface Gd³⁺ of the UGNP, confirming the surface-coating of the UGNP with the PAA. In the FT-IR absorption spectrum of the RGD-PAA-UGNP, the N-H bend and C-N stretch (labelled using vertical bars) were present, confirming the conjugation of the RGD to the PAA of the PAA-UGNP.

confirming the successful conjugation of the RGD to the PAA of the PAA-UGNP through the amide bond.

The elemental analysis (EA) also supported the surface-coating of the UGNPs with RGD-PAA. The measured C/H/O/N was 24.685/3.882/23.539/1.063 in wt% and 27.08/51.10/19.37/1.00 in mole ratio. Summing all these wt% provided 53.169, which was fairly consistent with the 46.6% estimated from the TGA curve (Fig. S2 in ESI†). It was estimated that eight or nine PAAs were grafted on each UGNP from the grafting density analysis^{49,50} and TGA data, and three or four RGDs were conjugated to each PAA-UGNP from the amounts of Gd-precursor and RGD used in the synthesis (ESI†). The C/H/O/N mole ratio estimated from EA was fairly well reproduced using the above-estimated numbers of PAAs and RGDs per RGD-PAA-UGNP (ESI†), confirming the reliability of these estimations. These estimations were also consistent with strong absorption intensities of PAA and RGD observed in the FT-IR absorption spectra of PAA-UGNPs and RGD-PAA-UGNPs (Fig. 3).

Estimated water proton relaxivities

The estimated r_1 and r_2 values of the RGD-PAA-UGNPs in an aqueous solution were 13.28 ± 0.07 and $15.51 \pm 0.71 \text{ s}^{-1} \text{ mM}^{-1}$,

respectively, from the $1/T_1$ and $1/T_2$ plots *versus* the Gd concentration (Fig. S3 in ESI[†]). These values were approximately 3 times higher than those of a commercial molecular contrast agent Gadovist⁵¹ which were also measured for reference (Fig. S3 in ESI[†]). Higher r_1 values of the surface-modified GNPs than those of Gd-chelates had been observed by many others^{52–60} and are primarily due to dense population of Gd³⁺ per nanoparticle whereas Gd-chelates have only one Gd³⁺ per molecule.

Thermal neutron beam irradiation time determination

The thermal neutron beam irradiation time was determined by estimating the maximal accumulation time of Gd at the cancer site. To this end, T_1 MR images of a mouse before and after the IV administration were measured for 2 h. The T_1 MR images taken before and 20 min after the IV administration are presented in Fig. 4a, and they displayed the high positive contrast enhancement at the cancer tissue due to the accumulation of Gd at the cancer site. The signal-to-noise ratio (SNR) of a region of interest (ROI) at the cancer site was plotted as a function of time in Fig. 4b, exhibiting that the contrast nearly reached the maximum at approximately 20 min after the IV administration and then nearly maintained at that value for up to 2 h, likely due to targeting of the cancer by the RGD-PAA-UGNPs. Therefore, the thermal neutron beam irradiation time was determined as 20 min after the IV administration. The contrast-to-noise ratios (CNRs) estimated from T_1 MR images as a function of time were plotted in Fig. 4c. This plot approximately represents Gd-amounts at various organs as a function of time because the CNR is approximately proportional to the Gd-amount.

In vitro cellular toxicity

As shown in Fig. 5, the RGD-PAA-UGNPs exhibited high cell viabilities in NCTC1469 normal cells and U87MG cancer cells up to 500 μ M Gd. Therefore, they were used for *in vivo* T_1 MRI and *in vivo* GdNCT.

Amount of Gd accumulated at the cancer site

To estimate the amount of Gd accumulated at the cancer site, the mice were sacrificed at three time points after the IV administration ($N = 3$ at each time point), and the cancer tissue was extracted. Inductively-coupled plasma atomic emission spectroscopy (ICPAES) was carried out to estimate the amount of Gd accumulated at the extracted cancer tissue. The result was plotted as a function of time in Fig. 6. The accumulated amount of Gd at the cancer site was maximal 20 min after the IV administration, and then it slightly decreased with time, which was nearly consistent with the time evolution of contrast changes in T_1 MR images shown in Fig. 4b. This accumulation of Gd was likely due to the delivery of hundreds of Gd per nanoparticle of the RGD-PAA-UGNPs and their cancer-targeting ability. In addition, their good transport properties through blood vessels, their cancer cell penetration due to their ultrasmall size, and their enhanced permeability and retention (EPR) effect⁶¹ would contribute to

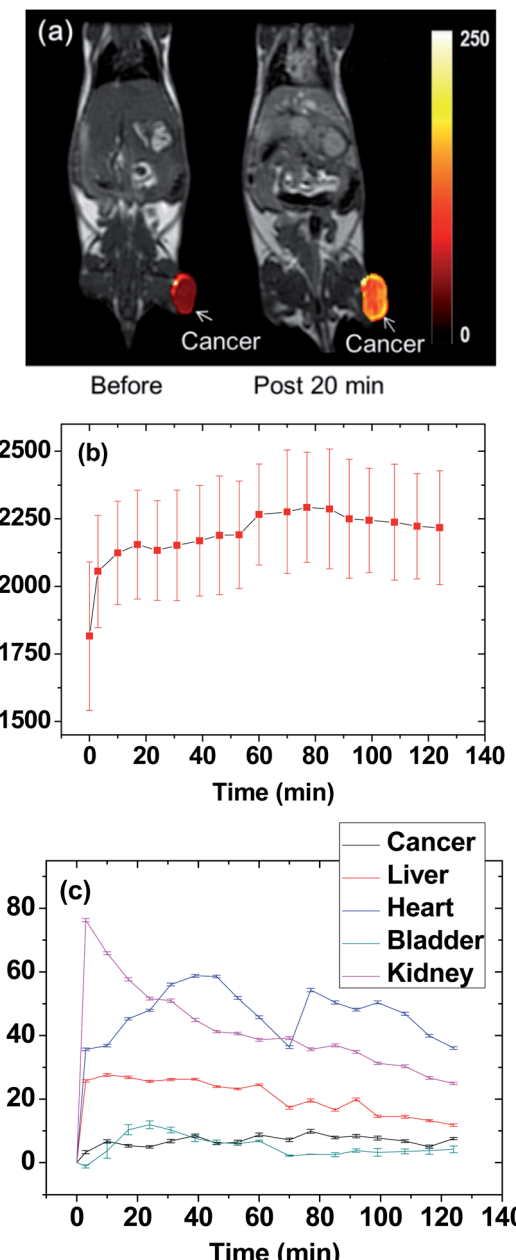


Fig. 4 Determination of the thermal neutron beam irradiation time from the maximal contrast at the cancer site from the T_1 MR images. (a) T_1 MR images before and 20 min after (labelled as "post 20 min") IV administration of the solution sample: a bright contrast at the cancer was due to the accumulation of Gd at the cancer site. (b) Plot of SNR-ROI at the cancer site in the T_1 MR images as a function of time ($N = 1$). (c) CNR plots of various organs as a function of time ($N = 1$).

the accumulation of Gd at the cancer site. However, the Gd-amount accumulated at the cancer site was not high compared to those in other organs (Fig. 4c), likely because only three or four RGDs were conjugated to each nanoparticle as mentioned before (also see ESI[†]). Therefore, to improve the accumulation of Gd at the cancer site, conjugation of more amount of RGDs to the NPs or better targeting ligands need to be tried for cancer targeting in future experiments.



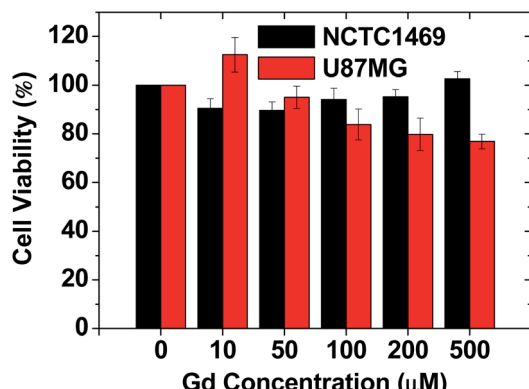


Fig. 5 The cytotoxicity of the RGD-PAA-UGNPs in NCTC1469 and U87MG cell lines.

In vivo GdNCT results

The overall scheme and concise explanation of the *in vivo* GdNCT experiment are provided in Fig. 1. To this end, the four mice groups [(i) Gd-*n*-: the mice group treated with no sample and with no thermal neutron beam, (ii) Gd+*n*-: the mice group treated with sample and with no thermal neutron beam, (iii) Gd-*n*+: the mice group treated with no sample and with thermal neutron beam, and (iv) Gd+*n*+: the mice group treated with sample and with thermal neutron beam] ($N = 5$ for each group) were prepared, and their cancer growths were monitored for 25 days by measuring the cancer volumes using a digital caliper. In addition, T_1 MR images and photographs of the four mice groups were taken before and after thermal neutron beam irradiation (Fig. S4 in ESI†), and those of the Gd-*n*- and Gd+*n*- mice groups are representatively provided in Fig. 7a, showing that the Gd+*n*- mice group had a significantly smaller cancer growth than that of the Gd-*n*- control mice group, due to the GdNCT effect.

The cancer volumes (V) normalized with respect to those (V_0) before thermal neutron beam irradiation (*i.e.*, V/V_0) were plotted as a function of day for the four mice groups (Fig. 7b). As shown in Fig. 7b, the Gd-*n*- control mice group exhibited the highest

cancer growth, corresponding to a natural cancer growth, whereas the Gd+*n*- mice group showed the lowest cancer growth due to the GdNCT effect. On the other hand, both the Gd+*n*- and Gd-*n* mice groups exhibited lower cancer growths than that of the Gd-*n*- control mice group, and higher cancer growths than that of the Gd+*n*- mice group. For an ideal case, it is expected that both the Gd+*n*- and Gd-*n* mice groups should have cancer growths similar to that of the Gd-*n*- control mice group, given that the RGD-PAA-UGNPs and thermal neutrons should not harm the cancer cells on their own. The former case is likely due to the slight cytotoxicity of the injected RGD-PAA-UGNPs for the U87MG cancer cells which were used in the inoculation of the nude mice, as noticed by cellular cytotoxicity tests (Fig. 5). A similar reduced cancer growth resulting from the injected commercial Gd-chelate based nanocomposites was observed by others.³² The latter case is probably due to the background capture of thermal neutrons by body elements such as ^1H (0.333 barns), ^{12}C (0.0035 barns), ^{14}N (1.83 barns), ^{16}O (0.00019 barns), ^{31}P (0.18 barns), and ^{35}Cl (32.68 barns),²⁹ as observed by others.^{28,29,31,32} This indicates that low thermal neutron beam irradiation doses should be used to avoid cell damage by thermal neutrons on their own. It should be noted that the Gd+*n*- mice group exhibited a cancer volume decrease (*i.e.*, $V/V_0 < 1.0$) for 16 days after the thermal neutron beam irradiation with a minimum of $V/V_0 = 0.3$ at day 5. This implies that all the cancer cells can be completely killed by repeated GdNCT treatments. After day 16, the Gd+*n*- mice group exhibited a slight cancer volume increase, which was significantly lower than those of the other three mice groups. At day 25, the values of V/V_0 of the four mice groups were compared (Fig. 7c). The Gd+*n*- mice group yielded the smallest V/V_0 among the four mice groups ($p^* < 0.05$, compared with the Gd-*n*- mice group), confirming the GdNCT effects of the RGD-PAA-UGNPs on the cancer: the Gd+*n*- group exhibited a 9% higher V/V_0 than the combined V/V_0 value of the Gd-*n*- and Gd+*n*- groups. Therefore, there is definitely GdNCT effect on the cancer growth suppression. It is expected that the GdNCT effect will increase by increasing the accumulated amount of Gd at the cancer site.

It should be noted that the surface-coating and cancer-targeting ligands of the UGNPs play an important role in GdNCT performance because transport properties, cancer-targeting ability, cancer cell penetration of the UGNPs depend on them. In this study, the PAA polymer and RGD molecule were used as surface-coating and cancer-targeting ligands, respectively. Therefore, different types of surface-coating and cancer-targeting ligands can be tried in an attempt to improve the GdNCT effects.

Experimental

Chemicals

$\text{GdCl}_3 \cdot x\text{H}_2\text{O}$ (99.9%), PAA (MW = 1800 amu; analytical standard grade), tetrahydrofuran (THF) (>99.9%), triethylene glycol (TEG) (99%), NaOH (>99.9%), *N*-(3-dimethylaminopropyl)-*N*'-ethylcarbodiimide hydrochloride (EDC·HCl) (99%), *N*-hydroxysuccinimide (NHS) (98%), and linear RGD (*i.e.*, Arg-Gly-Asp)

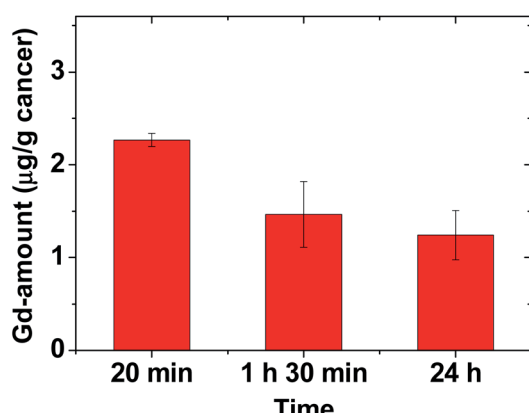


Fig. 6 Plot of Gd-amount accumulated at the cancer site at three time points ($N = 3$ at each time point).



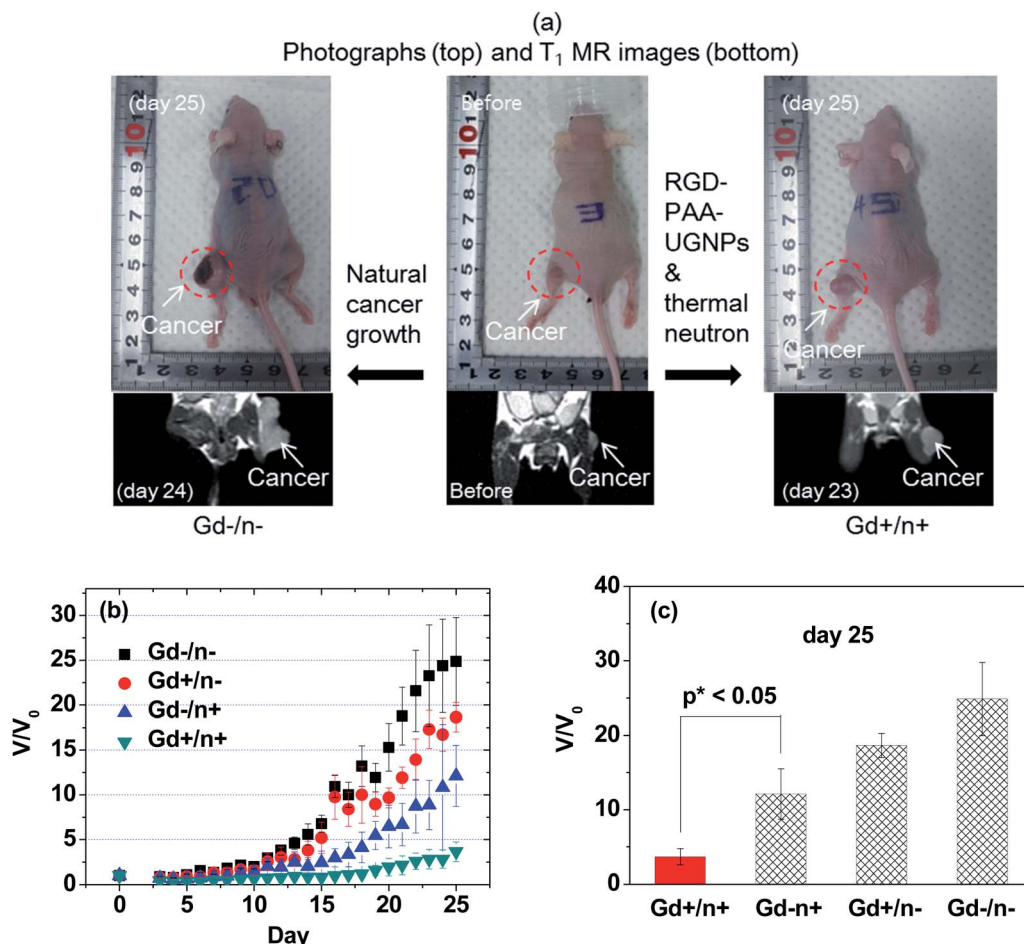


Fig. 7 *In vivo* GdNCT results. (a) Photographs and T_1 MR images of the Gd-/n- and Gd+/n+ mice groups before and day 23 or 24 or 25 after thermal neutron beam irradiation: the photographed mice were not necessarily the same as those subjected to MRI, but they belonged to the same mice group. (b) Plots of V/V_0 before and after the thermal neutron beam irradiation as a function of day ($N = 5$ for each mice group). (c) Plots of V/V_0 at day 25 after thermal neutron beam irradiation for the four mice groups ($p^* < 0.05$, $N = 5$ for each mice group).

(97%) were purchased from Sigma-Aldrich, USA, and used without further purification. Ethanol (>99%, Duksan, South Korea) was used for the initial washing of the nanoparticles. Triple-distilled water was used for the final washing of the nanoparticles and in the preparation of the aqueous solution sample.

Synthesis of PAA-coated UGNPs (*i.e.*, synthesis of PAA-UGNPs)

A mixture of $\text{GdCl}_3 \cdot x\text{H}_2\text{O}$ (2 mmol) and PAA (0.25 mmol) were magnetically stirred in 20 mL of TEG in a three-necked flask at 60 °C for 2 h under atmospheric conditions to obtain a clear precursor solution (Fig. 8a). In a separate beaker, 10 mmol of NaOH in 10 mL of TEG was prepared and then, added slowly to the precursor solution until a pH of 9–11 was reached. The mixed solution was magnetically stirred at 110 °C for 12 h and then, cooled to room temperature. The solution was transferred to a beaker and filled with 400 mL of ethanol. The solution was magnetically stirred for 10 min at room temperature and kept in a refrigerator for 3 days until the PAA-UGNPs settled to the bottom of the beaker. The clear supernatant solution was

decanted, and the remaining solution was washed again using 400 mL of ethanol. This washing process was repeated three times to remove Na^+ , Cl^- , TEG, unreacted PAA, and unreacted precursor from the solution containing the PAA-UGNPs. Then, 400 mL of triple-distilled water was added to the sample, and the solution was rotary evaporated to approximately 50 mL to remove ethanol. This process was repeated three times. The solution was dialyzed (MWCO = 2000 Da) against triple-distilled water (1.5 L) for 1 day to remove any remaining unreacted chemicals.

Conjugation of RGD to PAA-UGNPs (*i.e.*, synthesis of RGD-PAA-UGNPs)

Three-quarters of the above-synthesized PAA-UGNPs, EDC·HCl (1 mmol), and NHS (1 mmol) were added to 20 mL of triple-distilled water (pH = 6.0) and then, magnetically stirred for 1 h at room temperature under atmospheric conditions (Fig. 8b). The pH of the solution was increased to 7.2 by adding 0.1 M NaOH solution and then, 0.029 mmol of RGD was added to the solution. The solution was magnetically stirred for 12 h.



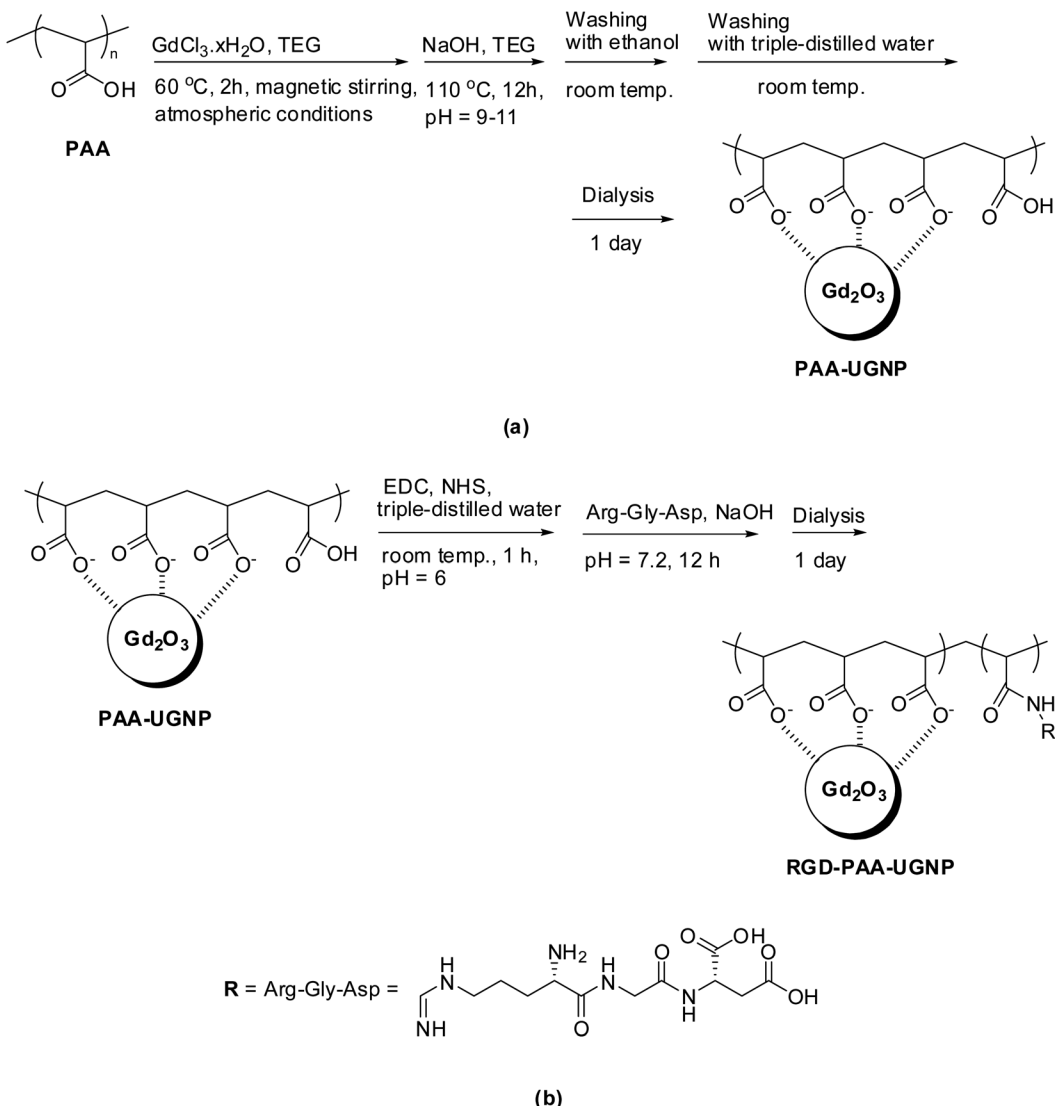


Fig. 8 Syntheses of (a) the PAA-UGNPs and (b) RGD-PAA-UGNPs.

The solution was dialyzed (MWCO = 2000 Da) against triple-distilled water (1.5 L) for 1 day to remove free EDC·HCl, NHS, and RGD from the solution containing the RGD-PAA-UGNPs.

General characterizations

The particle diameter of the RGD-PAA-UGNPs prepared on a copper grid after dispersion in ethanol was measured using an HRTEM instrument (Titan G2 ChemiSTEM CS Probe, FEI, Hillsboro, OR, USA) operated at an accelerating voltage of 200 kV. The Gd-concentration of the solution sample was determined *via* ICPAES (IRIS/AP, Thermo Jarrell Ash Co., Franklin, MA, USA). The hydrodynamic diameter was determined using a dynamic light scattering (DLS) particle size analyzer (UPA-150, Microtrac, San Diego, CA, USA) with a solution sample (approximately 0.05 mM Gd). The crystal structure of the powder sample before and after the TGA was measured using a powder XRD spectrometer (X-PERT PRO MRD, Philips, Eindhoven, The Netherlands) with unfiltered $\text{CuK}\alpha$ ($\lambda = 1.54184 \text{ \AA}$) radiation. The surface-coating of

the UGNPs was investigated by recording FT-IR absorption spectra (Galaxy 7020 A, Mattson Instruments, Inc., Madison, WI, USA) using powder samples pelletized in KBr. The amount of surface-coating on the UGNP surfaces was estimated by recording a TGA curve (SDT-Q 600, TA Instruments, New Castle, DE, USA). Because organic compounds burn out below 400°C , the TGA curve was scanned between room temperature and 900°C in an air flow. The amount of surface-coating was estimated from the mass drop in the TGA curve after the subtraction of the initial mass drop between the room temperature and approximately 105°C due to water and air desorption. An EA instrument (ThermoFisher, Flash 2000, Waltham, MA, USA) was also used to analyze the surface-coating amount and surface-coating composition (C, H, O, N) of a powder sample.

In vitro cytotoxicity measurements

The *in vitro* cytotoxicity of the solution sample was measured using a CellTiter-Glo Luminescent Cell Viability Assay



(Promega, Madison, WI, USA). The intracellular adenosine triphosphate (ATP) was quantified using a Victor 3 luminometer (PerkinElmer, Waltham, MA, USA). Two cell lines, *i.e.* normal mouse hepatocyte (NCTC1469) and U87MG were used. Each cell line was seeded onto a separate 24-well cell culture plate and incubated for 24 h (5×10^4 cell density, 500 μ L cells per well, 5% CO₂, and 37 °C). Five dilute solution samples containing the RGD-PAA-UGNPs were prepared by the dilution of the concentrated solution sample with a sterile phosphate-buffered saline (PBS) solution. Each of the cells was treated with 2 μ L of each diluted solution sample and the final Gd concentrations in the treated cells were 10, 50, 100, 200, and 500 μ M Gd. The treated cells were then incubated for 48 h. Cell viabilities were measured three times to obtain the average cell viabilities, which were then normalized with respect to that of untreated control cells (0.0 mM Gd).

Water proton relaxivity measurements

The longitudinal (T_1) and transverse (T_2) relaxation times were measured using a 1.5 T MRI scanner (GE 1.5 T Signa Advantage, GE Medical Systems, Chicago, IL, USA) equipped with a knee coil (MSK-Extreme, ONI Medical Systems, Inc., Wilmington, MA, USA). Five aqueous dilute solutions containing the RGD-PAA-UGNPs (1, 0.5, 0.25, 0.125, and 0.0625 mM Gd) were prepared by the dilution of the concentrated solution sample with triple-distilled water. These dilute solutions were used to measure both the T_1 and T_2 relaxation times. The T_1 relaxation times were measured using an inversion recovery method. In this method, the inversion time (TI) was varied at 1.5 T, and the MR images were acquired at 35 different TI values in the range of 50–1750 ms. The T_1 relaxation times were obtained from the nonlinear least-square fits to the measured signal intensities at various TI values. To measure the T_2 relaxation times, the Carr-Purcell-Meiboom-Gill pulse sequence was used for multiple spin-echo measurements. 34 images were acquired at 34 different echo time (TE) values in the range of 10–1900 ms. The T_2 relaxation times were obtained from the nonlinear least-square fits to the mean pixel values for the multiple spin-echo measurements at various TE values. The longitudinal (r_1) and transverse (r_2) water proton relaxivities of the solution sample were estimated from the slopes of the plots of $1/T_1$ and $1/T_2$, respectively, *versus* the Gd-concentration.

Animal experiments

All the *in vivo* animal experiments were approved by the animal research committee of the Kyungpook National University (KNU) and conducted in accordance with its rules. *In vivo* GdNCT experiments were approved by the animal research committee of the Korea Institute of Radiological & Medical Science (KIRAMS) and carried out in accordance with its rules.

Cancer model nude mice preparation

The U87MG cancer cells were incubated for 24 h at 37 °C in air containing 5% CO₂. Roswell Park Memorial Institute (RPMI-1640, Hyclone™, GE healthcare life sciences, USA) containing 10% (v/v) of fetal bovine serum (FBS) and 1% (v/v) of penicillin

streptomycin was used as the culture medium of the cells. BALB/c nude mice (male, 5 week old, 16–20 g) were given inoculation into subcutaneous (sc) tissue in left hind legs with 5×10^6 U87 MG cancer cells suspended in 100 μ L of phosphate saline solution. All the *in vivo* experiments including MRI and GdNCT were carried out three weeks after the cancer cell inoculations.

In vivo T_1 MR image measurements

In vivo T_1 MR images were obtained using a 1.5 T MRI scanner and homemade small animal radiofrequency (RF) coil. The coil was of the receiver type with an inner diameter of 50 mm. For measurements, the cancer model nude mice were anesthetized using 1.5% isoflurane in oxygen. The solution sample containing the RGD-PAA-UGNPs was IV administered as a bolus (0.1 mmol Gd per kg) into the mice tails. The T_1 MR images were acquired before and after the administration of the solution sample. The imaging parameters for the spin echo (SE) were as follows; repetition time (TR) = 300 ms; echo time (TE) = 13 ms; field of view (FOV) = 10 mm; matrix size = 192 × 160 pixel; slice thickness = 1 mm; and number of acquisition (NEX) = 8.

In vivo GdNCT experiments

The thermal neutron beam was generated using an MC-50 cyclotron (MC50, Scanditronix, Sweden) by irradiating the proton beam of 35 MeV onto the beryllium target (Fig. S5 in ESI†). The generated thermal neutron beam dose was set as 1.0 Gy/12 min.

For all the four cancer model nude mice groups, $N = 5$ was used. The solution sample containing the RGD-PAA-UGNPs was IV administered as a bolus (0.1 mmol kg⁻¹) into the tails of the cancer model nude mice. 20 min after the IV administration, the mice were locally irradiated with a thermal neutron beam dose of 0.3 Gy (4 min irradiation). Only the cancer sites were exposed to the thermal neutron beam and the other body parts of the mice were shielded using a thick Teflon plate (Fig. S6 in ESI†). The cancer sizes were directly measured using a digital caliper before and after the thermal neutron beam irradiation. The T_1 MR images and photographs were also measured. These measurements continued with day intervals up to day 25 after the thermal neutron beam irradiation. The cancer volume (V) was estimated using the following formula: $V = \text{length} \times \text{width} \times \text{height}$.

Statistical analysis

The cancer growth of the four mice groups was expressed as the mean and standard deviation (SD) and the significance of the results was confirmed by a *t*-test ($p^* < 0.05$ was considered statistically important).

Conclusions

In this study we demonstrated for the first time the successful applications of the surface-modified UGNPs ($d_{\text{avg}} = 1.8$ nm) to the *in vivo* GdNCT of cancer using the cancer model nude mice. To this end, the UGNPs were grafted with the surface-coating

ligand PAA for biocompatibility and colloidal stability, and then conjugated with the cancer-targeting ligand RGD. The RGD-PAA-UGNPs were accumulated at the cancer site and consequently, showed the GdNCT effect on the cancer. This result was probably due to the very high thermal neutron capture cross sections of ^{157}Gd and ^{155}Gd , and many outstanding properties of the RGD-PAA-UGNPs such as their delivery of hundreds of Gd atoms per nanoparticle to the cancer site, cancer-targeting ability, and ultrasmall size which allows good transport through blood vessels and cancer cell penetration. This study indicates that the surface-modified UGNPs with cancer-targeting ligands could be the potential and promising materials applicable to the *in vivo* GdNCT of cancer. Different types of cancer-targeting ligands can be tried in an attempt to improve the GdNCT effects of the UGNPs.

Author contribution statement

S. L. H. synthesized and characterized the samples and wrote the draft manuscript; G. C. and H.-K. K. prepared the cancer model nude mice and performed the MRI and GdNCT experiments; H. Y., X. M., M. Y. A., S. M., A. G., and S. L. assisted with the synthesis and characterization of the samples; K.-H. J., J. A. P., M. H. K., Y. J. L., and J. Y. K. prepared the thermal neutron beam experiments and assisted with GdNCT experiments; K.-S. C. performed the cellular toxicity experiments; Y. C. and G. H. L. led the project and G. H. L. wrote the manuscript.

Conflicts of interest

There are no conflicts to declare.

Acknowledgements

This study was supported by the Basic Science Research Program (Grant No. 2017R1A2B3003214 to YC and 2016R1D1A3B01007622 to GHL) and the Basic Research Laboratory (BRL) Program (Grant No. 2013R1A4A1069507) of the National Research Foundation funded by the Ministry of Education, Science, and Technology. We would like to thank the Korea Basic Science Institute for allowing us to use their XRD machine.

Notes and references

- 1 P. Caravan, J. J. Ellison, T. J. McMurry and R. B. Lauffer, *Chem. Rev.*, 1999, **99**, 2293–2352.
- 2 R. B. Lauffer, *Chem. Rev.*, 1987, **87**, 901–927.
- 3 J.-L. Bridot, A.-C. Faure, S. Laurent, C. Rivière, C. Billotey, B. Hiba, M. Janier, V. Josserand, J.-L. Coll, L. V. Elst, R. Mueller, S. Roux, P. Perriat and O. Tillement, *J. Am. Chem. Soc.*, 2007, **129**, 5076–5084.
- 4 J. Y. Park, M. J. Baek, E. S. Choi, S. T. Woo, J. H. Kim, T. J. Kim, J. C. Jung, K. S. Chae, Y. Chang and G. H. Lee, *ACS Nano*, 2009, **3**, 3663–3669.
- 5 G. Leinweber, D. P. Barry, M. J. Trbovich, J. A. Burke, N. J. Drindak, H. D. Knox, R. V. Ballad, R. C. Block, Y. Danon and L. I. Severnyak, *Nucl. Sci. Eng.*, 2006, **154**, 261–279.
- 6 N. S. Hosmane, J. A. Maguire, Y. Zhu and M. Takagaki, *Boron and Gadolinium Neutron Capture Therapy for Cancer Treatment*, World Scientific, Singapore, 2012.
- 7 C. Salt, A. J. Lennox, M. Takagaki, J. A. Maguire and N. S. Hosmane, *Russ. Chem. Bull.*, 2004, **53**, 1871–1888.
- 8 A. Deagostino, N. Protti, D. Alberti, P. Boggio, S. Bortolussi, S. Altieri and S. G. Crich, *Future Med. Chem.*, 2016, **8**, 899–917.
- 9 Y. Chang, K. S. Chae and G. H. Lee, *Bioinspired, Biomimetic Nanobiomater.*, 2016, **5**, 167–170.
- 10 H. S. Choi, W. Liu, P. Misra, E. Tanaka, J. P. Zimmer, B. I. Ipe, M. G. Bawendi and J. V. Frangioni, *Nat. Biotechnol.*, 2007, **25**, 1165–1170.
- 11 M. Longmire, P. L. Choyke and H. Kobayashi, *Nanomedicine*, 2008, **3**, 703–717.
- 12 J. F. Hainfeld, D. N. Slatkin, T. M. Focella and H. M. Smilowitz, *Br. J. Radiol.*, 2006, **79**, 248–253.
- 13 J. L. Shih and R. M. Brugger, *Med. Phys.*, 1992, **19**, 733–744.
- 14 U. M. Le and Z. Cui, *Int. J. Pharm.*, 2006, **312**, 105–112.
- 15 G. De Stasio, D. Deepika Rajesh, P. Casalbore, M. J. Daniels, R. J. Erhardt, B. H. Frazer, L. M. Wiese, K. L. Richter, B. R. Sonderegger, B. Gilbert, S. Schaub, R. J. Cannara, J. F. Crawford, M. K. Gilles, T. Tyliszczak, J. F. Fowler, L. M. Larocca, S. P. Howard, D. Mercanti, M. P. Mehta and R. Pallini, *Neurology Res.*, 2005, **27**, 387–398.
- 16 G. De Stasio, P. Casalbore, R. Pallini, B. Gilbert, F. Sanita, M. T. Ciotti, G. Rosi, A. Festinesi, L. M. Larocca, A. Rinelli, D. Perret, D. W. Mogk, P. Perfetti, M. P. Mehta and D. Mercanti, *Cancer Res.*, 2001, **61**, 4272–4277.
- 17 S. Barua and S. Mitragotri, *Nano Today*, 2014, **9**, 223–243.
- 18 A. Verma, O. Uzun, Y. Hu, Y. Hu, H.-S. Han, N. Watson, S. Chen, D. J. Irvine and F. Stelacci, *Nat. Mater.*, 2008, **7**, 588–595.
- 19 E. Oh, J. B. Delehanty, K. E. Sapsford, K. Susumu, R. Goswami, J. B. Blanco-Canosa, P. E. Dawson, J. Granek, M. Shoff, Q. Zhang, P. L. Goering, A. Huston and L. Medintz, *ACS Nano*, 2011, **5**, 6434–6448.
- 20 T. Wang, J. Bai, X. Jiang and G. U. Nienhaus, *ACS Nano*, 2012, **6**, 1251–1259.
- 21 H. Zhang, Q. Ji, C. Huang, S. Zhang, B. Yuan, K. Yang and Y.-Q. Ma, *Sci. Rep.*, 2015, **5**, 10525–10535.
- 22 M. Y. Ahmad, M. W. Ahmad, H. Cha, I. T. Oh, T. Tegafaw, X. Miao, S. L. Ho, S. Marasini, A. Ghazanfari, H. Yue, H.-K. Ryeom, J. Lee, K. S. Chae, Y. Chang and G. H. Lee, *Eur. J. Inorg. Chem.*, 2018, **26**, 3070–3079.
- 23 P. Mi, N. Dewi, H. Yanagie, D. Kokuryo, M. Suzuki, Y. Sakurai, Y. Li, I. Aoki, K. Ono, H. Takahashi, H. Cabral, N. Nishiyama and K. Kataoka, *ACS Nano*, 2015, **9**, 5913–5921.
- 24 K.-H. Jung, J. Y. Park, J. Y. Kim, M. H. Kim, S. Y. Oh, H.-K. Kim, E.-J. Choi, H.-J. Kim, S. H. Do, K. C. Lee, K. M. Kim, Y. J. Lee and Y. Chang, *Contrast Media Mol. Imaging*, 2018, 3727109.
- 25 R. F. Barth, J. A. Coderre, M. G. H. Vicente and T. E. Blue, *Clin. Cancer Res.*, 2005, **11**, 3987–4002.



26 H. Tokumitsu, J. Hiratsuka, Y. Sakurai, T. Kobayashi, H. Ichikawa and Y. Fukumori, *Cancer Lett.*, 2000, **150**, 177–182.

27 N. Dewi, P. Mi, H. Yanagie, Y. Sakurai, Y. Morishita, M. Yanagawa, T. Nakagawa, A. Shinohara, T. Matsukawa, K. Yokoyama, H. Cabral, M. Suzuki, Y. Sakurai, H. Tanaka, K. Ono, N. Nishiyama, K. Kataoka and H. Takahashi, *J. Cancer Res. Clin. Oncol.*, 2016, **142**, 767–775.

28 V. F. Khokhlov, P. N. Yashkin, D. I. Silin, E. S. Djorova and R. Lawaczeck, *Acad. Radiol.*, 1995, **2**, 393–398.

29 B. Hofmann, C.-O. Fisher, R. Lawaczeck, J. Platzek and W. Semmler, *Invest. Radiol.*, 1999, **34**, 126–133.

30 Y. Akine, N. Tokita, K. Tokuyue, M. Satoh, Y. Fukumori, H. Tokumitsu, R. Kanamor, T. Kobayashi and K. Kanda, *J. Cancer Res. Clin. Oncol.*, 1992, **119**, 71–73.

31 H. Ichikawa, T. Uneme, T. Andoh, Y. Arita, T. Fujimoto, M. Suzuki, Y. Sakurai, H. Shinto, T. Fukasawa, F. Fujii and Y. Fukumori, *Appl. Radiat. Isot.*, 2014, **88**, 109–113.

32 N. Dewi, H. Yanagie, H. Zhu, K. Demachi, A. Shinohara, K. Yokoyama, M. Sekino, Y. Sakurai, Y. Morishita, N. Iyomoto, T. Nagasaki, Y. Horiguchi, Y. Nagasaki, J. Nakajima, M. Ono, K. Kakimi and H. Takahashi, *Biomed. Pharmacother.*, 2013, **67**, 451–457.

33 V. N. Mitin, V. N. Kulakov, V. F. Khokhlov, I. N. Sheino, A. M. Arnopolskaya, N. G. Kozlovskaya, K. N. Zaitsev and A. A. Portnov, *Appl. Radiat. Isot.*, 2009, **67**, S299–S301.

34 E. S. Yim, B. Zhao, D. Myung, L. C. Kourtis, C. W. Frank, D. Carter, R. L. Smith and S. B. Goodman, *J. Biomed. Mater. Res., Part A*, 2009, **91**, 894–902.

35 E. Psarra, U. König, M. Müller, E. Bittrich, K.-J. Eichhorn, P. B. Welzel, M. Stamm and P. Uhlmann, *ACS Omega*, 2017, **2**, 946–958.

36 S. L. Ho, H. Cha, I. T. Oh, K.-H. Jung, M. H. Kim, Y. J. Lee, X. Miao, T. Tegafaw, M. Y. Ahmad, K. S. Chae, Y. Chang and G. H. Lee, *RSC Adv.*, 2018, **8**, 12653–12665.

37 K. M. Krueger, A. M. Al-Somali, M. Mejia and V. L. Colvin, *Nanotechnology*, 2007, **18**, 475709.

38 A. M. Smith and S. Nie, *J. Am. Chem. Soc.*, 2008, **130**, 11278–11279.

39 F. Söderlind, H. Pedersen, R. M. Petoral, P. O. Käll and K. Uvdal, *J. Colloid Interface Sci.*, 2005, **288**, 140–148.

40 K. Kattel, J. Y. Park, W. Xu, H. G. Kim, E. J. Lee, B. A. Bony, W. C. Heo, J. J. Lee, S. Jin, J. S. Baeck, Y. Chang, T. J. Kim, J. E. Bae, K. S. Chae and G. H. Lee, *ACS Appl. Mater. Interfaces*, 2011, **3**, 3325–3334.

41 The cell constant (a) = 10.813 Å, JCPDS-International Centre for Diffraction Data, card no. 43-1014, PCPDFWIN, vol. 1.30, 1997.

42 R. G. Pearson, *J. Am. Chem. Soc.*, 1963, **85**, 3533–3539.

43 R. G. Pearson, *J. Chem. Educ.*, 1968, **45**, 581–587.

44 R. G. Pearson, *J. Chem. Educ.*, 1968, **45**, 643–648.

45 O. W. Duckworth and S. T. Martin, *Geochim. Cosmochim. Acta*, 2001, **65**, 4289–4301.

46 S. J. Hug and D. Bahnemann, *J. Electron Spectrosc. Relat. Phenom.*, 2006, **150**, 208–219.

47 S. J. Hug and B. Sulzberger, *Langmuir*, 1994, **10**, 3587–3597.

48 C. B. Mendive, T. Bredow, M. A. Blesa and D. W. Bahnemann, *Phys. Chem. Chem. Phys.*, 2006, **8**, 3232–3247.

49 M. K. Corbierre, N. S. Cameron and R. B. Lennox, *Langmuir*, 2004, **20**, 2867–2873.

50 D. N. Benoit, H. Zhu, M. H. Lilierose, R. A. Verm, N. Ali, A. N. Morrison, J. D. Fortner, C. Avendano and V. L. Colvin, *Anal. Chem.*, 2012, **84**, 9238–9245.

51 Gadobutrol, Bayer Scherring Pharma, Germany.

52 J. Y. Park, Y. Chang and G. H. Lee, *Curr. Med. Chem.*, 2015, **22**, 569–581.

53 T. J. Kim, K. S. Chae, Y. Chang and G. H. Lee, *Curr. Top. Med. Chem.*, 2013, **13**, 422–433.

54 W. Xu, K. Kattel, J. Y. Park, Y. Chang, T. J. Kim and G. H. Lee, *Phys. Chem. Chem. Phys.*, 2012, **14**, 12687–12700.

55 M. Engström, A. Klasson, H. Pedersen, C. Vahlberg, P.-O. Käll and K. Uvdal, *Magn. Reson. Mater. Phys., Biol. Med.*, 2006, **19**, 180–186.

56 M.-A. Fortin, R. M. Petoral Jr, F. Söderlind, A. Klasson, M. Engström, T. Veres, P.-O. Käll and K. Uvdal, *Nanotechnology*, 2007, **18**, 395501.

57 J. Miyawaki, M. Yudasaka, H. Imai, H. Yorimitsu, H. Isobe, E. Nakamura and S. Iijima, *J. Phys. Chem. B*, 2006, **110**, 5179–5181.

58 M. Ahrén, L. Selegård, A. Klasson, F. Söderlind, N. Abrikossova, C. Skoglund, T. Bengtsson, M. Engström, P.-O. Käll and K. Uvdal, *Langmuir*, 2010, **26**, 5753–5762.

59 A.-A. Guay-Bégin, P. Chevallier, L. Faucher, S. Turgeon and M.-A. Fortin, *Langmuir*, 2012, **28**, 774–782.

60 M. A. McDonald and K. L. Watkin, *Acad. Radiol.*, 2006, **13**, 421–427.

61 Y. Matsumura and H. Meada, *Cancer Res.*, 1986, **46**, 6387–6392.

